



ARL-TR-8965 • MAY 2020



Control Actuation Requirements Development for Munitions

by Joshua T Bryson, Benjamin C Gruenwald, Joseph D Vasile,
Frank E Fresconi

Approved for public release; distribution is unlimited.

NOTICES

Disclaimers

The findings in this report are not to be construed as an official Department of the Army position unless so designated by other authorized documents.

Citation of manufacturer's or trade names does not constitute an official endorsement or approval of the use thereof.

Destroy this report when it is no longer needed. Do not return it to the originator.



Control Actuation Requirements Development for Munitions

Joshua T Bryson, Benjamin C Gruenwald, Joseph D Vasile, and Frank E Fresconi

Weapons and Materials Research Directorate, CCDC Army Research Laboratory

REPORT DOCUMENTATION PAGE

*Form Approved
OMB No. 0704-0188*

Public reporting burden for this collection of information is estimated to average 1 hour per response, including the time for reviewing instructions, searching existing data sources, gathering and maintaining the data needed, and completing and reviewing the collection information. Send comments regarding this burden estimate or any other aspect of this collection of information, including suggestions for reducing the burden, to Department of Defense, Washington Headquarters Services, Directorate for Information Operations and Reports (0704-0188), 1215 Jefferson Davis Highway, Suite 1204, Arlington, VA 22202-4302. Respondents should be aware that notwithstanding any other provision of law, no person shall be subject to any penalty for failing to comply with a collection of information if it does not display a currently valid OMB control number.

PLEASE DO NOT RETURN YOUR FORM TO THE ABOVE ADDRESS.

1. REPORT DATE (DD-MM-YYYY) May 2020			2. REPORT TYPE Technical Report		3. DATES COVERED (From - To) 1 August–1 November 2019	
4. TITLE AND SUBTITLE Control Actuation Requirements Development for Munitions					5a. CONTRACT NUMBER	
					5b. GRANT NUMBER	
					5c. PROGRAM ELEMENT NUMBER	
6. AUTHOR(S) Joshua T Bryson, Benjamin C Gruenwald, Joseph D Vasile, and Frank E Fresconi					5d. PROJECT NUMBER	
					5e. TASK NUMBER	
					5f. WORK UNIT NUMBER	
7. PERFORMING ORGANIZATION NAME(S) AND ADDRESS(ES) CCDC Army Research Laboratory ATTN: FCDD-RLW-LE Aberdeen Proving Ground, MD 21005-5069					8. PERFORMING ORGANIZATION REPORT NUMBER ARL-TR-8965	
9. SPONSORING/MONITORING AGENCY NAME(S) AND ADDRESS(ES)					10. SPONSOR/MONITOR'S ACRONYM(S)	
					11. SPONSOR/MONITOR'S REPORT NUMBER(S)	
12. DISTRIBUTION/AVAILABILITY STATEMENT Approved for public release; distribution is unlimited.						
13. SUPPLEMENTARY NOTES ORCID IDs: Joshua T Bryson, 0000-0002-0753-6823; Joseph D Vasile, 0000-0003-3812-6277						
14. ABSTRACT Enhancing munition maneuverability is a key enabling technology for long-range precision munitions that supports both range extension and terminal maneuvers. One approach to munition maneuverability is to deflect control surfaces to achieve body attack angles that generate lift from the body and other aerodynamic surfaces. This work presents a methodology to analyze aerodynamic control surfaces to develop actuator requirements to ensure the control actuation system has sufficient torque to overcome aerodynamic loading and sufficient bandwidth to stabilize the projectile dynamics. These methodologies are demonstrated in this report on a gun-launched, aerodynamically stabilized, fin-controlled projectile, but are applicable to other control-surface design problems.						
15. SUBJECT TERMS fin control projectile, optimal flight control, actuator requirements, actuator bandwidth, actuator torque						
16. SECURITY CLASSIFICATION OF:			17. LIMITATION OF ABSTRACT UU	18. NUMBER OF PAGES 24	19a. NAME OF RESPONSIBLE PERSON Joshua T Bryson	
a. REPORT Unclassified	b. ABSTRACT Unclassified	c. THIS PAGE Unclassified			19b. TELEPHONE NUMBER (Include area code) (410) 306-1939	

Contents

List of Figures	iv
List of Tables	iv
1. Introduction	1
2. Airframe	1
3. Aerodynamic Model	3
4. Control-Surface Design Methodology	5
5. Actuator Requirements: Torque	7
6. Actuator Requirements: Bandwidth	9
7. Conclusion	14
8. References	15
List of Symbols, Abbreviations, and Acronyms	16
Nomenclature	17
Distribution List	18

List of Figures

Fig. 1	Projectile’s flight body; dimensions are in millimeters.	2
Fig. 2	Numbering scheme and deflection sign convention for the trailing-edge control surfaces compared with the body-fixed coordinate system. View is from projectile base.	3
Fig. 3	Comparison of a) the aerodynamic body coordinate frame for the aerodynamic coefficients and b) the flight dynamics coordinate frame for the calculated forces and moments.....	5
Fig. 4	Trim α across Mach for varying pitch deflection angles for the 8- and 12-cm control surfaces. The α corresponding to the maximum lift-to-drag is plotted in black.....	6
Fig. 5	Pitch deflection schedule across Mach to optimize lift-to-drag ratio for the 8- and 12-cm control surface designs. Both designs achieve similar α to optimize lift-to-drag, but the 12-cm control surface generally requires smaller deflections than the 8-cm design.	6
Fig. 6	Coefficient of aerodynamic hinge load experienced by actuator 1 at optimal δq and projectile trim α across Mach for the 8- and 12-cm control surface.....	7
Fig. 7	Aerodynamic hinge moment experienced at the actuator for control surface 1 at optimal δq and optimal projectile trim α across Mach for the 8- and 12-cm control surface designs at sea level, 5 km, and 10-km altitude.....	8
Fig. 8	Achievable performance estimates for 2-Nm actuator torque limit for both the 8- and 12-cm control surface across Mach for several flight altitudes. The limited actuator torque limits the achievable δ , in 8a and 8b, which limits the achievable α trim, 8c and 8d, resulting in suboptimal CL/CD , 8e and 8f.	9
Fig. 9	Example step response for flight controllers after tuning across Mach, altitude, and control surface size, demonstrating desired 0.8-s rise time	12
Fig. 10	Frequency response for tuned flight controllers. The gain and phase margin, as well as the crossover frequencies, are included for each condition.	13
Fig. 11	Frequency response for flight controller tuned to Mach 0.8 with the altitude at sea level and a 12-cm control surface. The actuator dynamics included with three decreasing natural frequency values...	14

List of Tables

Table 1	Projectile mass properties	2
---------	----------------------------------	---

1. Introduction

Recent emphasis has been placed on investigating technologies and methodologies that can extend the range of guided munitions to provide better coverage of the battlefield. Range extension improvements can be achieved through rocket propulsion and gun propellant technology to increase projectile energy. Interior ballistics and propulsion technology research are being leveraged to extend range through increased launch energy.¹

For a fixed launch energy, the munition range can be extended by enhancing the projectile maneuverability to generate lift through a positive body angle of attack, enabling range extension through gliding flight²⁻⁴ as well as terminal maneuvers. Projectile maneuverability is influenced by the airframe design and aerodynamics as well as the design and implementation of control surfaces.²⁻⁴ Active research into low-drag high-lift airframes for both supersonic and subsonic flight regimes is improving the understanding of desirable features of the airframe design while reducing design-cycle iteration time to rapidly evolve capabilities.⁵

This report presents a methodology to analyze control surface designs and their effect on the projectile to estimate torque and bandwidth requirements for the actuator to drive the control surface by 1) analyzing the aerodynamic hinge load that must be overcome by the actuator and 2) by sweeping the natural frequency of a second-order actuator model and analyzing the effect on the performance of the flight controller. This research is illustrated on a generic fin-controlled projectile, but the approach is applicable to other control-surface design problems.

2. Airframe

The characteristics of the projectile outer-mold line were shaped through a series of optimization analyses that identified design candidates with low drag and high lift-to-drag ratios.⁵ The optimization study focused on fin-stabilized designs to improve maneuverability of the projectile. The projectile is designed to be sabot-launched from an 8-inch-diameter gun using a smoothbore barrel or slip-band obturator. The projectile has no deploying aerodynamic surfaces after launch. The 8-inch-diameter gun requirement constrains the optimization to limit the fin span to 8 inches tip to tip. The optimized control surface design for a given body baseline configuration with a 105-mm diameter, 10-cal. length, and ogive length of 30% of the overall length of the projectile is shown in Fig. 1. The design was optimized to maximize lift to drag, minimize drag, and meet a desired static margin value (i.e., 0.3) across supersonic Mach regime ($M = 1-4$) at an 8° body

angle attack. This 8° body angle was selected based on preliminary trim angle predictions for the vehicle with trailing-edge flap deflections. Table 1 shows the projectile's mass properties.

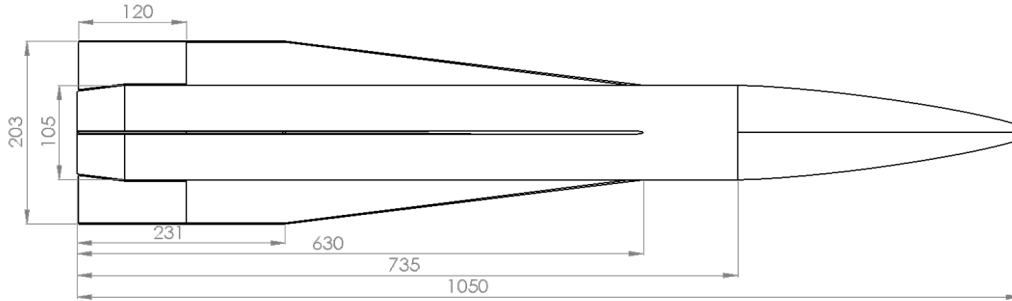


Fig. 1 Projectile's flight body; dimensions are in millimeters.

Table 1 Projectile mass properties

Mass	14.8 kg
CG_x	630 mm from nose
CG_y, CG_z	On center line
I_{xx}	0.0273 kg-m ²
I_{yy}, I_{zz}	1.17 kg-m ²

A trailing-edge flap on each of the four fins is rotated about the leading edge to provide control of the projectile during flight. Figure 1 shows the trailing-edge flap as 12 cm, but a variant with 8-cm trailing-edge flaps is also considered in this study. The aerodynamic forces and moments of the configuration were obtained using the semi-empirical aerodynamic prediction code Missile DATCOM (release 2014)⁶ and NASA's Cartesian Euler computational fluid dynamics (CFD) analysis package Cart3D (1.5.5).⁷ Only the drag and dynamic derivatives for the airframe were predicted using DATCOM, whereas all other forces and moments (pitching moment of airframe, normal force of trailing-edge flap, etc.) were predicted by Cart3D. The aerodynamic data for the trailing-edge flap components were found by simulating a single trailing-edge flap (i.e., Flap 3) in the cruciform orientation at multiple deflections (i.e., $\delta = 0^\circ, 5^\circ, 10^\circ, 15^\circ, 25^\circ,$ and 30°) across all flight conditions. The trailing-edge flap data were then applied to the other flaps (i.e., Flaps 1, 2, and 4) and combined with the rest of the airframe as discussed in Section 3. The numbering scheme of the control flaps and the deflection sign convention is presented in Fig. 2.

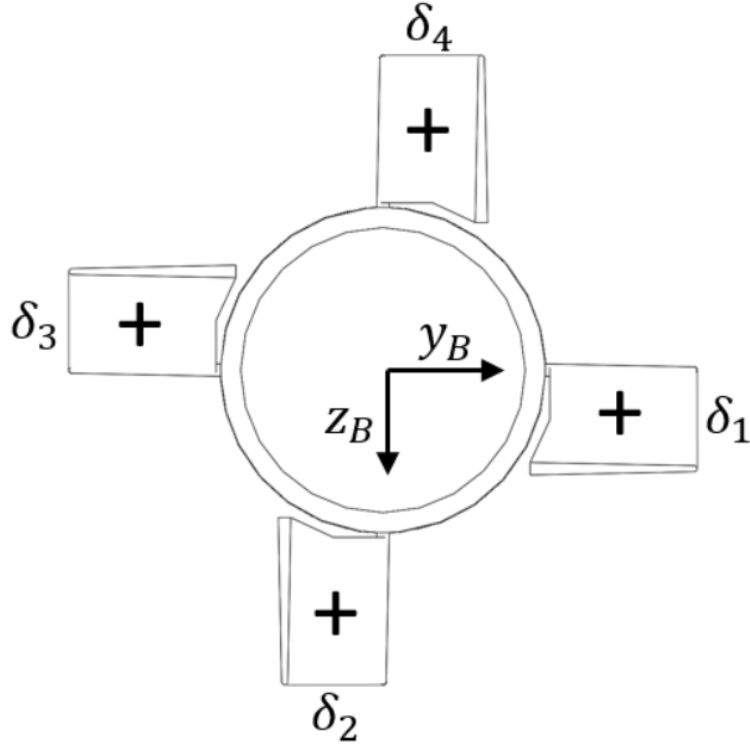


Fig. 2 Numbering scheme and deflection sign convention for the trailing-edge control surfaces compared with the body-fixed coordinate system. View is from projectile base.

3. Aerodynamic Model

The aerodynamic model provides the aerodynamic forces and moments at a given angle of attack and Mach number using aerodynamic coefficient data.^{8–10} Aerodynamic data describing the forces and moments due to the movable fin tabs, termed movable aerodynamic surfaces (MASs), are applied separately from the aerodynamic data for the assembly of the body and fixed fin surfaces, referred to as fixed aerodynamic surfaces (FASs).

The aerodynamic forces and moments from the FAS component are $[F_X \ F_Y \ F_Z]^T$ and $[M_L \ M_M \ M_N]^T$, respectively, and are given in Eqs. 1–6.

$$F_X = -QS [C_{X_0}(M) + C_{X_{\bar{\alpha}^2}}(M) \sin^2 \bar{\alpha}] \quad (1)$$

$$F_Y = -QS [C_{Y_\beta}(M) \sin \beta + C_{Y_{\beta^3}}(M) \sin^3 \beta + C_{Y_{\beta^5}}(M) \sin^5 \beta] \quad (2)$$

$$F_Z = -QS [C_{Z_\alpha}(M) \sin \alpha + C_{Z_{\alpha^3}}(M) \sin^3 \alpha + C_{Z_{\alpha^5}}(M) \sin^5 \alpha] \quad (3)$$

$$M_L = QSD \left[C_{l_0}(M) + C_{l_p}(M) \frac{pD}{2V} \right] \quad (4)$$

$$M_M = QSD \left[C_{m_\alpha}(M) \sin \alpha + C_{m_{\alpha^3}}(M) \sin^3 \alpha + C_{m_{\alpha^5}}(M) \sin^5 \alpha + C_{m_q}(M) \frac{qD}{2V} \right] \quad (5)$$

$$M_N = QSD \left[-C_{n_\beta}(M) \sin \beta - C_{n_{\beta^3}}(M) \sin^3 \beta - C_{n_{\beta^5}}(M) \sin^5 \beta + C_{n_r}(M) \frac{rD}{2V} \right] \quad (6)$$

where α is the body angle of attack, β is the body angle of sideslip, $\bar{\alpha} = \sqrt{\alpha^2 + \beta^2}$ is the total body angle of attack, D is the projectile diameter, V is the projectile velocity, $Q = \frac{1}{2} \rho V^2$ is the dynamic pressure, and $S = \frac{\pi}{4} D^2$ is the aerodynamic reference area.

The MAS aerodynamic model, given in Eqs. 7–12, sums the force and moment contributions of the four movable fin-flap surfaces arrayed around the body.

$$F_X^{MAS} = -QS \sum_{i=1}^4 \left[C_{X_0}^i(M, \delta_i) + C_{X_{\bar{\alpha}^2}}^i(M, \delta_i) \sin^2 \bar{\alpha} \right] \quad (7)$$

$$F_Y^{MAS} = -QS \sum_{i=1}^4 \left[C_{Y_\beta}^i(M, \delta_i) \sin \beta + C_{Y_{\beta^3}}^i(M, \delta_i) \sin^3 \beta + C_{Y_{\beta^5}}^i(M, \delta_i) \sin^5 \beta \right] \quad (8)$$

$$F_Z^{MAS} = -QS \sum_{i=1}^4 \left[C_{Z_\alpha}^i(M, \delta_i) \sin \alpha + C_{Z_{\alpha^3}}^i(M, \delta_i) \sin^3 \alpha + C_{Z_{\alpha^5}}^i(M, \delta_i) \sin^5 \alpha \right] \quad (9)$$

$$M_L^{MAS} = QSD \left[C_{l_\alpha}^1(M, \delta_1) \sin \alpha + C_{l_\beta}^2(M, \delta_2) \sin \beta + C_{l_\alpha}^3(M, \delta_3) \sin \alpha + C_{l_\beta}^4(M, \delta_4) \sin \beta \right] \quad (10)$$

$$M_M^{MAS} = QSD \sum_{i=1}^4 \left[C_{m_\alpha}^i(M, \delta_i) \sin \alpha + C_{m_{\alpha^3}}^i(M, \delta_i) \sin^3 \alpha + C_{m_{\alpha^5}}^i(M, \delta_i) \sin^5 \alpha \right] \quad (11)$$

$$M_N^{MAS} = QSD \sum_{i=1}^4 \left[-C_{n_\beta}^i(M, \delta_i) \sin \beta - C_{n_{\beta^3}}^i(M, \delta_i) \sin^3 \beta - C_{n_{\beta^5}}^i(M, \delta_i) \sin^5 \beta \right] \quad (12)$$

While the FAS model coefficients are only dependent on Mach number, the MAS aerodynamic model is populated with coefficients that depend on both Mach number and the deflection angle of the i^{th} control surface, δ_i . Both the FAS and MAS coefficients are calculated in the aerodynamic body coordinate frame, with +X out the tail, +Y right, and +Z up, as shown in Fig. 3a, and are converted to force and moments in the standard flight dynamics coordinate frame with +X out the nose, +Y right, and +Z down, as shown in Fig. 3b, through the formulation of Eqs. 1–12.

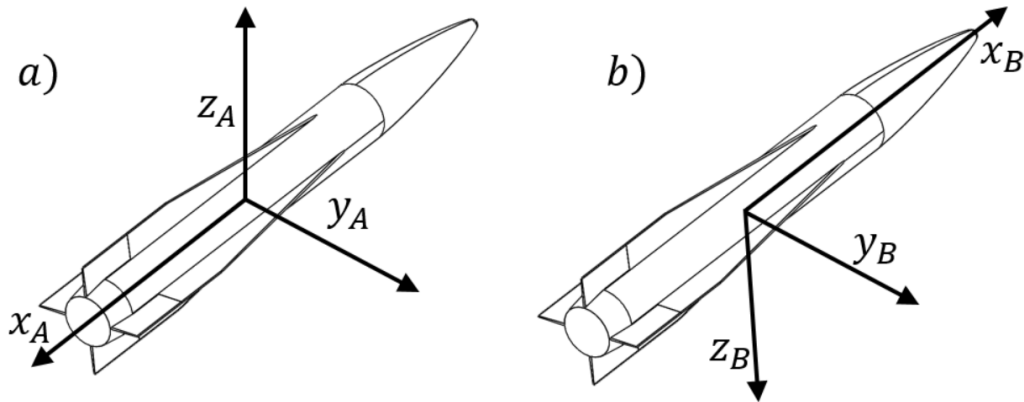


Fig. 3 Comparison of a) the aerodynamic body coordinate frame for the aerodynamic coefficients and b) the flight dynamics coordinate frame for the calculated forces and moments

4. Control-Surface Design Methodology

Once the coefficients have been developed to populate the aerodynamic model of the projectile FAS and MAS, an aerodynamic trim analysis is performed to determine the body angle of attack and lateral acceleration due to varying MAS deflections.^{11,12} Figure 4 shows how the trim α changes across Mach number for a set of given deflection angles. Note the lateral force and moment data are calculated using an inviscid flow solver and therefore do not predict flow separation (i.e., onset of stall) accurately; the higher body angles of attack in Fig. 4 are likely not achievable. Figure 5 facilitates comparisons between the 8- and 12-cm flap designs by plotting each pitch deflection schedule across Mach to achieve the optimal C_L/C_D ratio and the resulting body α . Both the 8- and 12-cm designs achieve similar α for optimal C_L/C_D , but the 12-cm control surface generally requires smaller deflections than the 8-cm design, as expected.

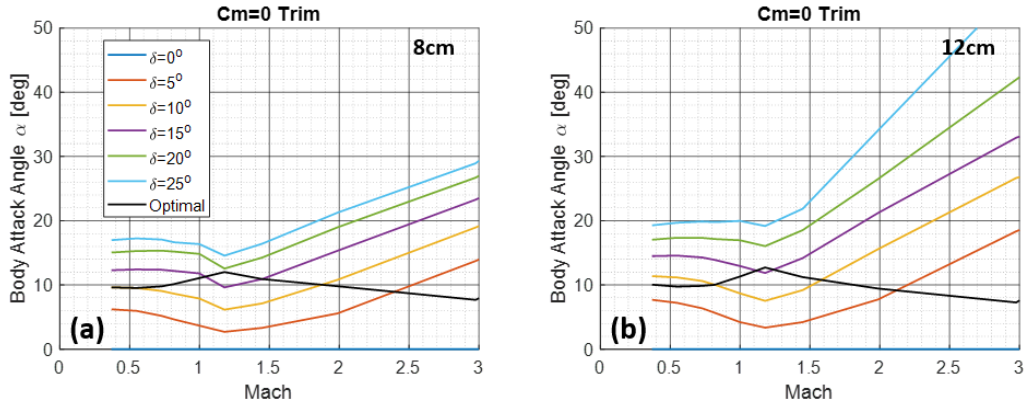


Fig. 4 Trim α across Mach for varying pitch deflection angles for the 8- and 12-cm control surfaces. The α corresponding to the maximum lift-to-drag is plotted in black.

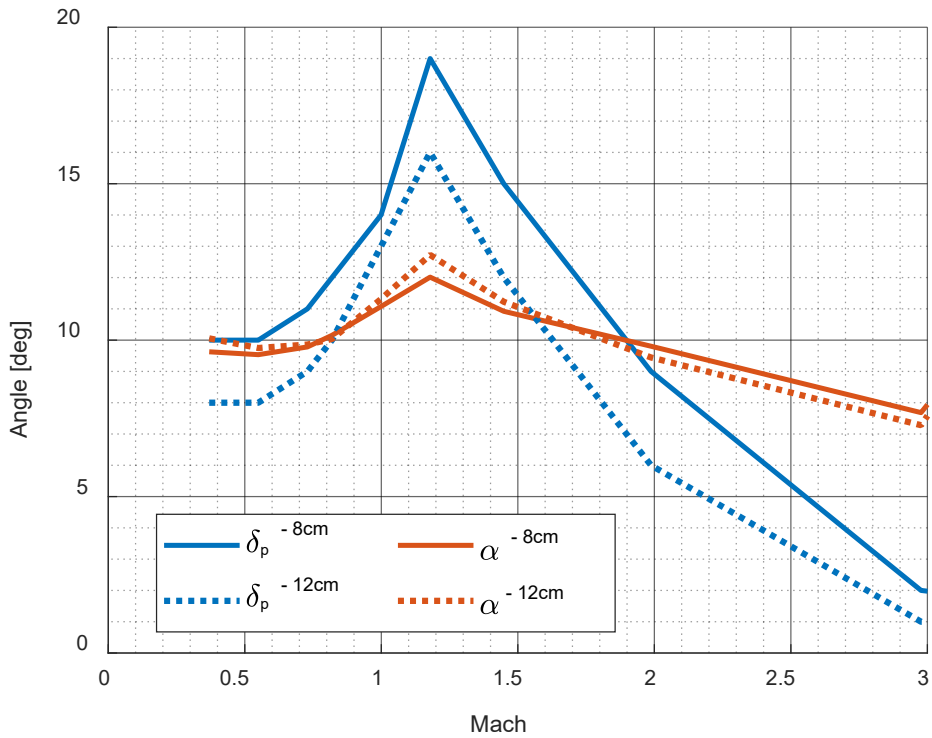


Fig. 5 Pitch deflection schedule across Mach to optimize lift-to-drag ratio for the 8- and 12-cm control surface designs. Both designs achieve similar α to optimize lift-to-drag, but the 12-cm control surface generally requires smaller deflections than the 8-cm design.

5. Actuator Requirements: Torque

The deflection of a control surface requires an actuator with sufficient mechanical torque to overcome the aerodynamic hinge moment induced by the airflow over the control surface. This induced hinge moment is calculated from the aerodynamic normal force on the control surface and the moment arm between the control surface hinge and the aerodynamic center of pressure (CP) of the control surface. Component-level aerodynamic analysis using an inviscid flow solver provides hinge moment coefficient for the i^{th} control surface, ${}^H C_m^i$, which is a function of Mach, α , β , and δ_i . The aerodynamic hinge moment can be obtained from the ${}^H C_m^i$ value:

$${}^H M^i = QSD[{}^H C_m^i(M, \alpha, \beta, \delta_i)] \quad (14)$$

Figure 6 plots ${}^H C_m^1$ for control surface 1 across Mach for the 8- and 12-cm designs. In each case the control surface held at the optimal δ_q with the projectile at the optimal trim angle, α , as previously shown in Fig. 5.

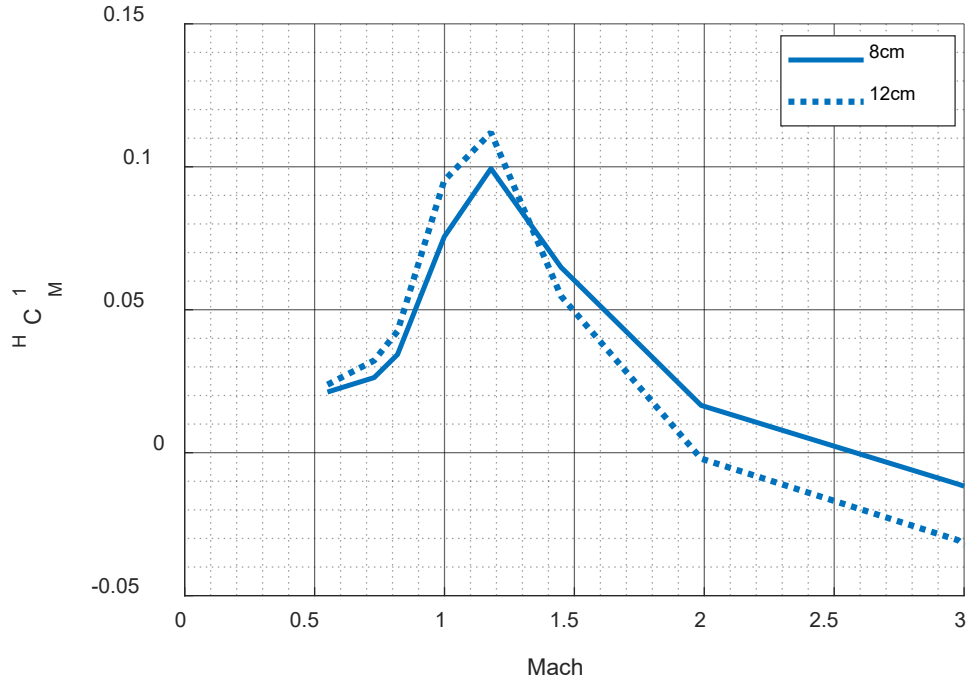


Fig. 6 Coefficient of aerodynamic hinge load experienced by actuator 1 at optimal δ_q and projectile trim α across Mach for the 8- and 12-cm control surface

Assuming constant density and speed of sound at a constant altitude, the dynamic pressure, Q , can be calculated across Mach for the projectile. Using these terms, and assuming the δ_p and α schedule given in Fig. 5, the aerodynamic moment

experienced at the actuator can be recovered from ${}^H C_m^1$. Figure 7 plots this hinge moment for control surface 1 at three different altitudes: sea level, 5 km, and 10 km. Both the 8- and 12-cm control surfaces require less than 2 Nm of actuator torque to overcome the aerodynamic forces at subsonic speeds. CP movement and higher dynamic pressure at high Mach number cause the 12-cm control surface to generate aerodynamic hinge moments of significantly higher magnitude at Mach 2–3. Overall, the hinge moment generated from the 8-cm control surface is flatter across supersonic Mach numbers, regardless of altitude. The large-magnitude destabilizing moments (shown as negative in Fig. 7) at higher Mach numbers are of particular concern for actuator design because they tend to cause deflection angles to increase, potentially destabilizing the projectile if the actuator is underpowered.

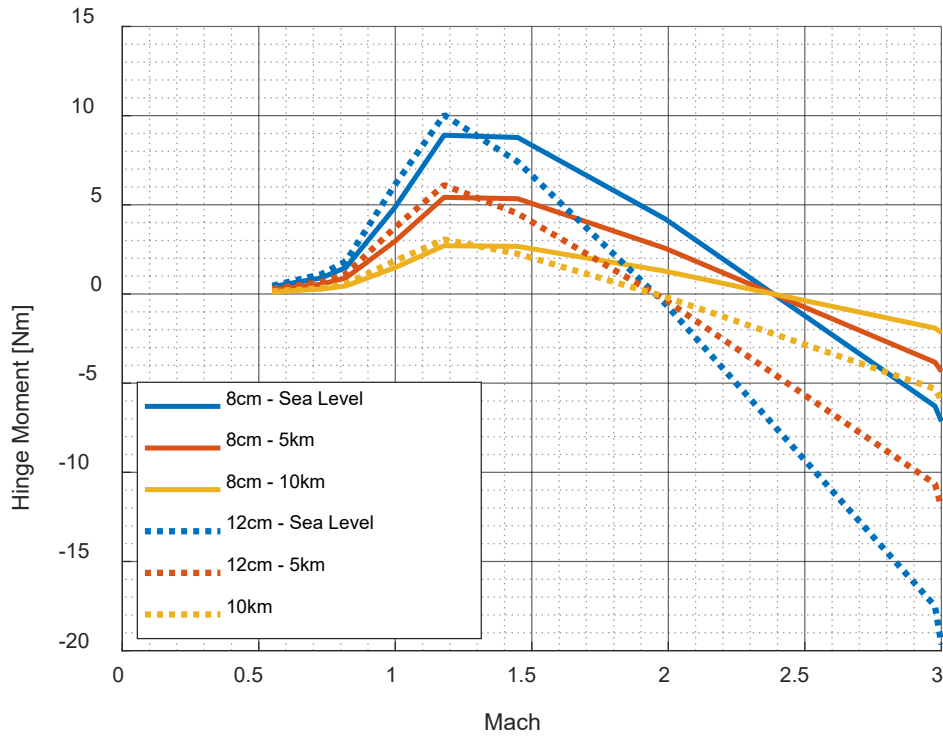


Fig. 7 Aerodynamic hinge moment experienced at the actuator for control surface 1 at optimal δ_q and optimal projectile trim α across Mach for the 8- and 12-cm control surface designs at sea level, 5 km, and 10-km altitude

Designing an actuator capable of enough output torque to overcome the aerodynamic hinge moments given in Fig. 7 is challenging, and the realized projectile maneuverability may be limited in part by the output torque capability of the actuator, particularly in the supersonic flight regimes. Figure 8 shows the impact to performance in the case of an actuator limited to 2-Nm output torque for both the 8- and 12-cm control surface designs. Figures 8a and 8b plot the 2-Nm torque-limited maximum deflection angles at different altitudes across Mach, along

with the optimal deflection angle goal shown in black. Figures 8c and 8d plot the resulting body trim α achieved by the limited δ for various flight altitudes along with the optimal α in black. Figures 8e and 8f plot the C_L/C_D ratio for the projectile for the achievable δ and α along with the optimal C_L/C_D in black. The 2-Nm actuator is able to drive both the 8- and 12-cm control surface designs to meet the optimal C_L/C_D in the subsonic flight regime but limits the achievable C_L/C_D in the transonic flight regime for both the 8- and 12-cm control surfaces. In the supersonic Mach 2–3 flight regime, both the 8- and 12-cm control surface designs are limited by the 2-Nm actuator, but the achievable C_L/C_D is better for the 8-cm design, especially as altitude is increased above sea level.

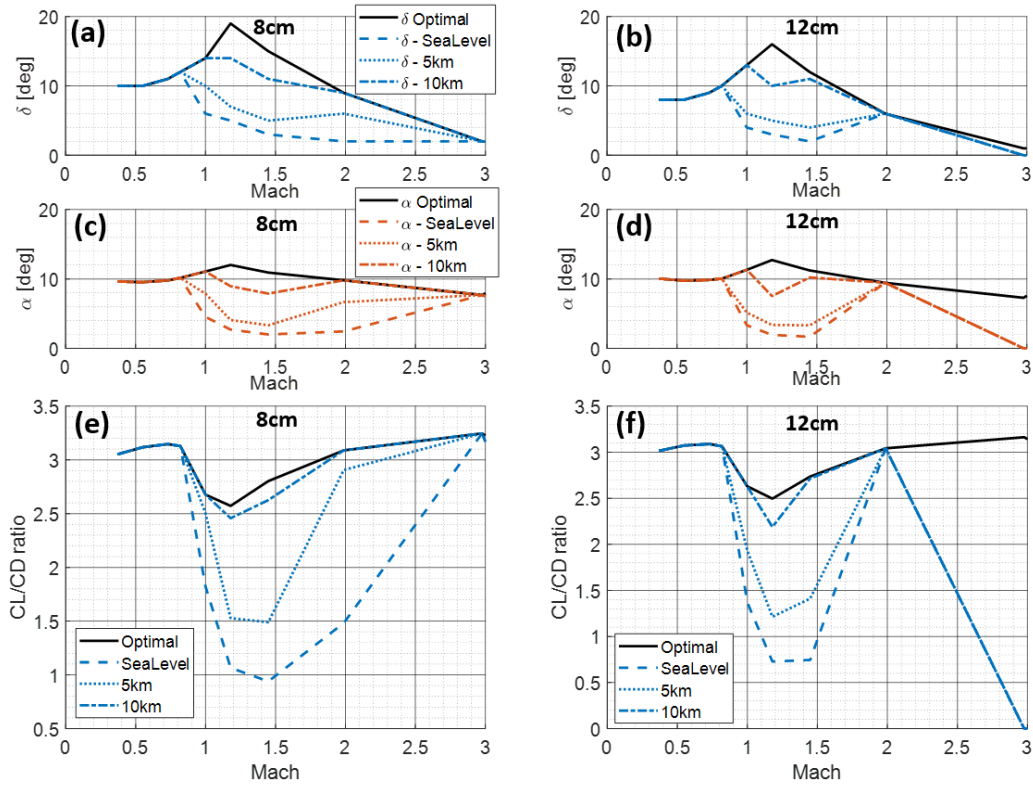


Fig. 8 Achievable performance estimates for 2-Nm actuator torque limit for both the 8- and 12-cm control surface across Mach for several flight altitudes. The limited actuator torque limits the achievable δ , in 8a and 8b, which limits the achievable α trim, 8c and 8d, resulting in suboptimal C_L/C_D , 8e and 8f.

6. Actuator Requirements: Bandwidth

In addition to the torque requirements for the actuator, the actuator bandwidth requirements can also be estimated for each of the control surface designs from the flight control design for the projectile. Since the actuator is the physical channel between the flight control algorithm and the projectile, it is necessary to first

understand the flight control requirements. The actuator bandwidth requirements can then be determined such that the flight control algorithm can be properly applied to the projectile. For this purpose, a linearized plant model of the projectile in the pitch plane is represented here as

$$\dot{x}_p(t) = A_p x_p(t) + B_p u(t) \quad (15)$$

with $x_p(t) = [q(t), \dot{w}(t)]^T$ being the plant state vector and $u(t) = [\delta_1(t), \delta_3(t)]^T$ being the pitch control input vector

$$A_p = \begin{bmatrix} \frac{QSD^2}{2I_{zz}V} C_{m_q} & \frac{mD}{I_{zz}} \frac{C_{m_\alpha}}{C_{z_\alpha}} \\ \frac{QS}{m} C_{z_\alpha} & -\frac{QS}{mV} C_{z_\alpha} \end{bmatrix}, \text{ and } B_p = \begin{bmatrix} -\frac{QSD}{2I_{zz}} C_{m_{\delta_q}} & \frac{QSD}{2I_{zz}} C_{m_{\delta_q}} \\ 0 & 0 \end{bmatrix}$$

Investigation of the airframe dynamics using available aerodynamics and mass properties indicates the roll dynamics are slightly slower than the pitch plane dynamics for this projectile. Additionally, the yaw dynamics are equivalent to the pitch dynamics due to symmetry, so the investigation of the pitch dynamics will reveal the overall actuator requirements.

The desired objective for the flight control is to track a desired pitch acceleration $\dot{w}_d(t)$ while regulating the pitch rate $q(t)$ to zero. This can be achieved by first augmenting the integrator dynamics given by

$$\dot{z}(t) = \dot{w}(t) - \dot{w}_d(t) \quad (16)$$

with the linearized plant dynamics (Eq. 15), which can be written as

$$\dot{x}(t) = Ax(t) + Bu(t) + B_r c(t) \quad (17)$$

where $x(t) = [x_p^T(t), z(t)]^T$ is the augmented state vector, $c(t) = \dot{w}_d(t)$ is the desired tracking command

$$A = \begin{bmatrix} \frac{QSD^2}{2I_{zz}V} C_{m_q} & \frac{mD}{I_{zz}} \frac{C_{m_\alpha}}{C_{z_\alpha}} & 0 \\ \frac{QS}{m} C_{z_\alpha} & -\frac{QS}{mV} C_{z_\alpha} & 0 \\ 0 & 1 & 0 \end{bmatrix}, \quad B = \begin{bmatrix} -\frac{QSD}{2I_{zz}} C_{m_{\delta_q}} & \frac{QSD}{2I_{zz}} C_{m_{\delta_q}} \\ 0 & 0 \\ 0 & 0 \end{bmatrix}, \text{ and } B_r = \begin{bmatrix} 0 \\ 0 \\ -1 \end{bmatrix}$$

The control law can then be designed as

$$u(t) = -Kx(t) \quad (18)$$

where linear quadratic regulator (LQR) theory can be used to design an appropriate gain K . The closed-loop controlled projectile model can now be written using Eq. 18 in Eq. 17 as

$$\dot{x}(t) = (A - BK)x(t) + B_r c(t) \quad (19)$$

The use of an LQR theory to design the feedback gain ensures all of the states in the state vector $x(t)$ are regulated to zero. Since this includes the integral error state $z(t) = \int (\dot{w}(t) - \dot{w}_d(t))dt$, it implies the desired commands are tracked as well.

For the designed control architecture, the method of obtaining an appropriate gain matrix K and then analyzing the requirements for the actuator bandwidth can now be discussed. First, an operating point is chosen where the model will be linearized. We illustrate this approach in this report for both a subsonic and supersonic case at Mach 0.8 and 2.5, respectively. For each flight speed we then consider three altitudes, at sea level, 5 km, and 10 km, and calculate a linear model for each flight speed–altitude pair using Vasile et al.⁵ The feedback gain K is then tuned using the linearized models for each Mach and altitude pairing for both the 8- and 12-cm control surfaces (i.e., 12 different cases). The tuning consists of placing weighting terms on the states and control to obtain the desired level of command following, while regulating the remaining states to zero, and minimizing the control effort.

The desired performance can be captured by analyzing the step response for the different cases. Figure 9 shows the achievable performance for the tuned controllers. It is evident the controller is tuned to achieve similar performance for the different Mach, altitude, and control-surface length combinations. It was desired that the rise times for each to be approximately 0.8 s, which can be seen from the time necessary to reach 0.9 in the amplitude. This dictates how quickly the flight controller causes the projectile to track a vertical acceleration command. By tuning the controllers to perform consistently between the different cases, we can then investigate how the demands on the actuator for proper application of the flight control law will change across the flight envelope and for different control-surface lengths.

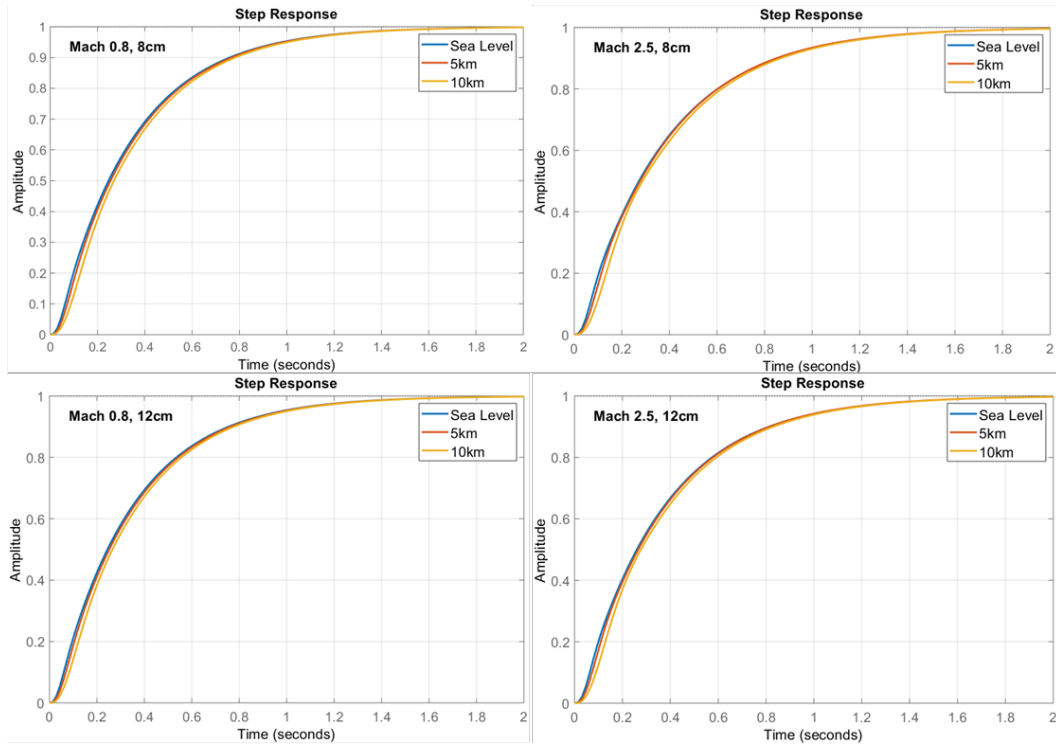


Fig. 9 Example step response for flight controllers after tuning across Mach, altitude, and control surface size, demonstrating desired 0.8-s rise time

To determine what is necessary from the actuator to achieve the desired performance, we use a frequency response analysis of the different cases in the form of Bode diagrams, as shown in Fig. 10. These are obtained by breaking the closed loop at the input and then looking separately at both fin-control surfaces (i.e., δ_1 and δ_3). Since there is symmetry between the two fins in controlling the pitch dynamics, the frequency responses are identical for each control channel; hence, we only consider one control channel. The frequency responses include the stability margins that are a measure of how robust the flight controllers are to uncertainties and unmodeled dynamics such as the actuator dynamics being considered. In particular, the phase margin (labeled Pm in the plots) is a measure of how much additional phase lag can be introduced into the system before instability occurs. In addition, the time delay margin can be computed from the phase margin and crossover frequency. It is a fairly common rule of thumb that the actuator dynamics should have a natural frequency five times the crossover frequency. This ensures the actuator dynamics are fast enough to allow for correct application of the flight control law through the actual physical control surfaces. Note in Fig. 10 how the stability margins change between different Mach and altitude conditions. Specifically, to obtain the same performance shown in Fig. 9, the crossover frequency increases as the altitude decreases from 10 km to sea level. This implies the actuator will need to be faster at lower altitudes as the higher air densities at

lower altitudes increase the dynamic pressure, requiring faster application of the flight control law. The speed of the projectile also plays a role in the actuator bandwidth requirement. The crossover frequencies are smaller for Mach 2.5 cases than for the Mach 0.8 cases. The size of the control surface also plays a role in the actuator bandwidth requirement as seen by the increase in crossover frequencies for increased control surface size from 8 to 12 cm.

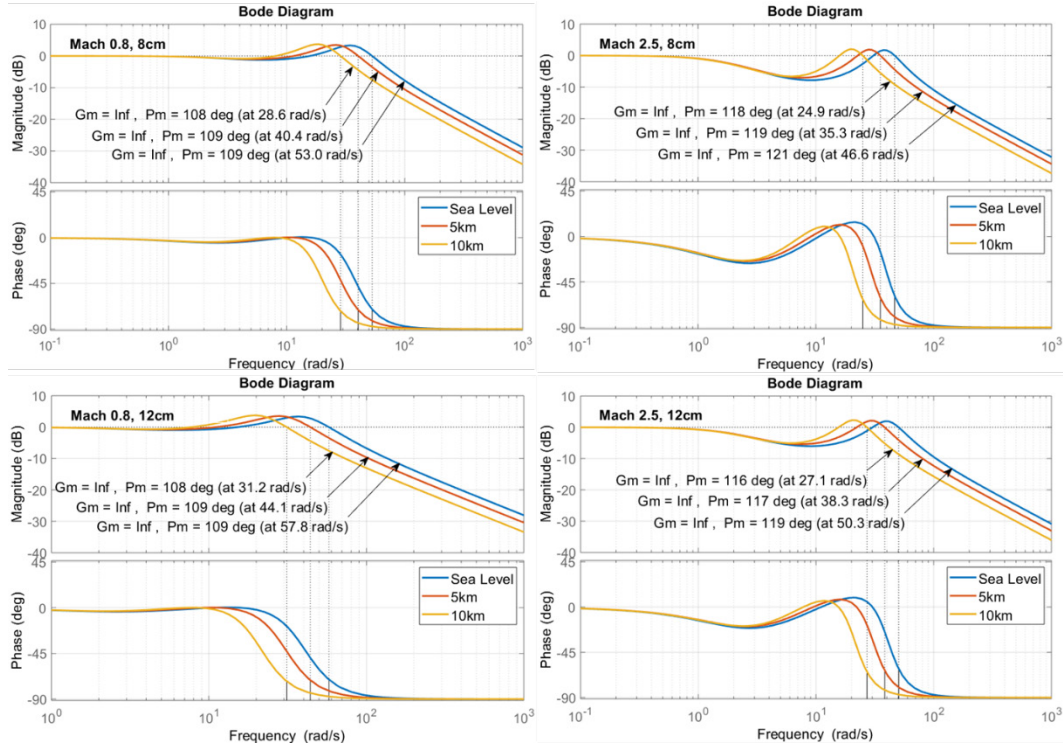


Fig. 10 Frequency response for tuned flight controllers. The gain and phase margin, as well as the crossover frequencies, are included for each condition.

For the cases considered, the largest crossover frequency occurs at 57.8 rad/s for the Mach 0.8, sea level, and 12-cm flap flight condition. This results in the required actuator bandwidth being approximately 300 rad/s or about 48 Hz. Figure 11 provides the frequency response for the Mach 0.8, sea level, and 12-cm flap case with the actuator dynamics included. We consider second-order actuator models with a damping ratio $\zeta = 1$ and decreasing natural frequencies, ω_n . It can be seen from Fig. 11 that at $\omega_n = 300$ rad/s there is still sufficient phase margin to ensure robustness to other unmodeled dynamics and uncertainties not considered. In addition, as the actuator dynamics become slower, the phase margin becomes negative, implying the system is unstable, as seen for the $\omega_n = 100$ rad/s case. Also note that the reverse of this process can also be considered. One can specify an actuator bandwidth and then design the flight controller to work with that specification. In this case the flight controller is tuned such that the crossover

frequency is a fifth of the natural frequency of the specified actuator dynamics. The tradeoff is that the achievable performance of the flight controller could then deteriorate.

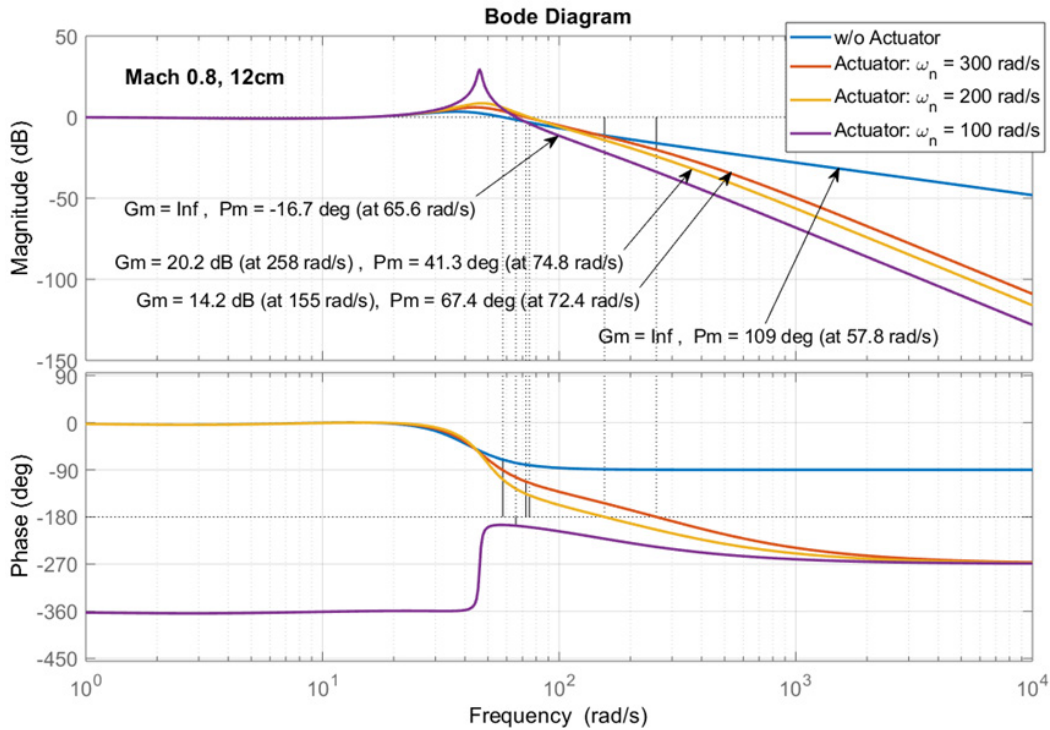


Fig. 11 Frequency response for flight controller tuned to Mach 0.8 with the altitude at sea level and a 12-cm control surface. The actuator dynamics included with three decreasing natural frequency values.

7. Conclusion

A methodology was presented to analyze an aerodynamic control surface design to estimate actuator requirements to ensure the control actuation system has sufficient torque to overcome in-flight aerodynamic loading and sufficient bandwidth to stabilize the projectile dynamics. These methodologies were demonstrated in this report on a gun-launched, aerodynamically stabilized, fin-controlled projectile.

Future work on this topic will include investigation of flight control performance with consideration for as-built actuator characteristics, along with expansion of the linear model to include sensor dynamics for state estimation. Additional aerodynamic studies are also planned with Navier-Stokes CFD simulations and wind tunnel testing to augment current estimates before beginning flight test evaluations.

8. References

1. Minnicino M, Sorensen B, Hepner DJ, Horst AW, Schmidt EM, Brandon FJ. Artillery range extension. Aberdeen Proving Ground (MD): Army Research Laboratory (US); 2010 Aug. Report No.: ARL-TR-5221.
2. Costello M. Extended range of a gun launched smart projectile using controllable canards. *Shock Vib.* 2001;8(3-4):203–213.
3. Fresconi FE. Range extension of gun-launched smart munitions. In: Bless S, editor. *Proceedings of the 24th International Symposium on Ballistics*; 2008 Sep 22–26; New Orleans, LA. Lancaster (PA): DEStech Publications, Inc; c2008. p. 157–164.
4. Bryson JT, Vasile JD, Celmins I, Fresconi FE. Approach for understanding range extension of gliding indirect fire munitions. *AIAA Scitech.* 2018;3158.
5. Vasile JD, Bryson JT, Fresconi FE. Aerodynamic design optimization of long range projectile using missile DATCOM. Reston (VA): AIAA Scitech. 2020;1762.
6. Rosema C, Doyle J, Blake W. *Missile DATCOM user's manual.* Wright-Patterson AFB (OH): Flight Dynamics Directorate, Air Force Research Laboratory (US); 2014 Dec. Report No.: AFRL-RQ-WP-TR-2014-0281.
7. Aftosmis MJ, Berger MJ, Adomavicius G. A parallel multilevel method for adaptively refined Cartesian grids with embedded boundaries. *Proceedings of the 38th Aerospace Sciences Meeting and Exhibit*; 2000 Jan 10–13; Reno, NV. Paper No.: AIAA-2000-0808.
8. McCoy RL. *Modern exterior ballistics.* Atglen (PA): Schiffer; 2012.
9. Fresconi FE, Celmins I, Sifton S, Costello M. High maneuverability projectile flight using low cost components. *Aerosp Sci Technol.* 2015;41:175–188.
10. Zipfel PH. *Modeling and simulation of aerospace vehicle dynamics.* AIAA education series. Reston (VA): American Institute of Aeronautics and Astronautics, Inc.; 2014.
11. Bryson JT, Vasile JD, Gruenwald BC, Fresconi FE. Control surface design analysis and actuation requirements development for munitions. *AIAA Scitech.* 2020;20.
12. Bryson JT, Vasile JD, Fresconi FE. Control surface design analysis for munitions. Aberdeen Proving Ground (MD): Army Research Laboratory (US); 2020 Mar. Report No.: ARL-TR-8919.

List of Symbols, Abbreviations, and Acronyms

ARL	Army Research Laboratory
CCDC	US Army Combat Capabilities Development Command
CFD	computational fluid dynamics
CP	center of pressure
FAS	fixed aerodynamic surfaces
LQR	linear quadratic regulator
MAS	movable aerodynamic surfaces
NASA	National Aeronautics and Space Administration

Nomenclature

α	=	body angle of attack in pitch plane
$\bar{\alpha}$	=	total body angle of attack, $\sqrt{\alpha^2 + \beta^2}$
β	=	body angle of sideslip in yaw plane
C_D	=	drag coefficient
C_L	=	lift coefficient
C_{l_0}	=	zeroth order roll moment coefficient
C_{l_p}	=	roll damping coefficient
C_m	=	coefficient of pitching moment
$C_{m_\alpha}, C_{m_{\alpha^3}}, C_{m_{\alpha^5}}$	=	first, third, and fifth order fit coefficients for aerodynamic pitching moment
C_{m_q}	=	pitch damping coefficient
$C_{n_\beta}, C_{n_{\beta^3}}, C_{n_{\beta^5}}$	=	first, third, and fifth order fit coefficients for aerodynamic yaw moment
C_{n_r}	=	yaw damping coefficient
$C_{X_0}, C_{X_{\bar{\alpha}^2}}$	=	zeroth and second order fit coefficients for X-axis aerodynamic force
$C_{Y_\alpha}, C_{Y_{\alpha^3}}, C_{Y_{\alpha^5}}$	=	first, third, and fifth order fit coefficients for Y-axis aerodynamic force
$C_{Z_\alpha}, C_{Z_{\alpha^3}}, C_{Z_{\alpha^5}}$	=	first, third, and fifth order fit coefficients for Z-axis aerodynamic force
$\delta_1, \delta_2, \delta_3, \delta_4$	=	deflection angles for control surface 1,2,3,4
δ_q	=	deflection of virtual/combined control surface for pitch
D	=	reference diameter
M	=	Mach number
p	=	roll rate
Q	=	$\frac{1}{2} \rho V^2$, dynamic pressure
q	=	pitch rate
r	=	yaw rate
S	=	$D^2\pi/4$, aerodynamic reference area
w	=	Z-axis velocity
\dot{w}	=	Z-axis acceleration

1 DEFENSE TECHNICAL
(PDF) INFORMATION CTR
DTIC OCA

1 CCDC ARL
(PDF) FCDD RLD CL
TECH LIB

16 CCDC ARL
(PDF) FCDD RLW A
F FRESCONI
FCDD RLW LE
J BRYSON
B GRUENWALD
J VASILE
I CELMINS
J DESPIRITO
L FAIRFAX
L STROHM
FCDD RLW L
T SHEPPARD
W OBERLE
FCDD RLW LB
N TRIVEDI
FCDD RLW LC
J SADLER
FCDD RLW LD
P CONROY
FCDD RLW LF
M ILG
B TOPPER
FCDD RLW LH
J NEWILL